

# A Qualitative Examination of Dynamic Stall from Flight Test Data

William G. Bousman  
 Research Scientist  
 U.S. Army Aeroflightdynamics Directorate (ATCOM)  
 Moffett Field, California

## Abstract

Three flight conditions from the UH-60A Airloads Program are examined where dynamic stall occurs on the rotor: a symmetric pull-up that includes non-zero angular rates and accelerations; a high-speed, diving turn that includes non-zero angular rates, but nominally zero angular accelerations; and a level flight case with zero angular rates and accelerations. The two maneuver conditions result in severe pitch-link loads and represent design conditions for this military aircraft. Dynamic stall characteristics are identified in the section lift, the section pitching moment, and the trailing edge pressure and are used to create rotor disk maps that show the location and behavior of dynamic stall for this rotor. The measured blade pressures are used to examine the dynamic stall process itself and airfoil maps are developed that show the behavior of the dynamic stall vortex on the blade and its interaction with areas of supercritical flow. It is shown that the torsional dynamics of the rotor control *where* dynamic stall may occur, while the flight condition and the resulting aerodynamic inflow determine *whether* it will occur.

## Notation

|   |                                  |
|---|----------------------------------|
| a   | speed of sound, ft/sec           |
| b   | number of blades                 |
| $C_L$   | lift coefficient                 |
| $C_{L_{max}}$   | maximum static lift coefficient  |
| $C_M$   | moment coefficient               |
| $C_{W/\sigma} = \frac{GW}{\pi\sigma\rho\Omega^2 R^4}$ | gross weight coefficient         |
| c   | blade chord, ft                  |
| GW  | aircraft gross weight, lbs       |
| g   | acceleration due to gravity      |
| L   | section normal force, lbs/in     |
| M   | local Mach number                |
| $M^2 C_L = \frac{2L}{\rho a^2 c}$                     | section normal force coefficient |

|   |   |
|---|---|
| $M^2 C_M = \frac{2M_t}{\rho a^2 c^2}$               | section pitching moment coefficient                             |
| $M^2 C_{pu} = \frac{2(p_u - p_\infty)}{\rho a^2 c}$ | upper surface pressure coefficient                              |
| $M_t$   | sect. pitching moment, in-lb/in                                 |
| $n_z$   | load factor, g  |
| $P/L_{osc}$   | oscillatory pitch-link force (half peak-to-peak), lbs           |
| p   | surface pressure, lbs/in <sup>2</sup>                           |
| $p_\infty$  | static pressure, lbs/in <sup>2</sup>                            |
| q   | pitch rate, deg/sec   |
| R   | blade radius, ft  |
| r   | radial coordinate, ft   |
| x   | chordwise coordinate, ft  |
| $\alpha$  | angle of attack, deg  |
| $\phi$  | induced flow angle, deg   |
| $\mu$   | advance ratio   |
| $\theta_{cont}$                                     | blade control angle, deg  |
| $\theta_{elas}$                                     | blade torsional deformation, deg                                |
| $\rho$  | air density, slug/ft <sup>3</sup>                               |
| $\sigma$  | rotor solidity, $bc/\pi R$                                      |
| $\Omega$  | rotor rotational speed, rad/sec                                 |
| $\psi$  | rotor azimuth, deg  |
| $\psi_{0.5c}$                                       | rotor azimuth where dynamic stall vortex crosses 50% chord, deg |

## Introduction

Dynamic stall on a helicopter rotor in high-speed or maneuvering flight causes large blade torsional moments and control system loads and, in some cases, will size control system components for a new aircraft design. The ability of present analyses to predict rotor loads under dynamic stall conditions is largely unsatisfactory. Analytical approaches to this problem have, as a first step, examined the modeling of dynamic stall on a two-dimensional (2D) basis. Much has been learned about the basic phenomenon from 2D wind tunnel testing (Ref. 1) and numerous empirical models have been developed that can be incorporated into conventional lifting-line analyses. In addition, recent calculations using a Navier-Stokes flow

Presented at the American Helicopter Society 53rd Annual Forum, Virginia Beach, Virginia, April 29–May 1, 1997. Copyright © 1997 by the American Helicopter Society, Inc. All rights reserved.

solver with a variety of turbulence models (Ref. 2) have shown promising results, but again for the 2D problem. Experiments on an oscillating wing in a wind tunnel have been used to assess the importance of three-dimensional dynamic stall effects (Ref. 3) and an initial evaluation, based on a variety of computational methods, suggests that 2D models are adequate for the computational task (Ref. 4). The recent availability of flight test data on a UH-60A, including measured blade pressures (Ref. 5) provides an opportunity to assess the accuracy of current analytical methods for the prediction of dynamic stall effects on an aircraft. A first step in the assessment process is a careful examination of the dynamic stall measurements obtained in flight. That assessment is the purpose of this paper.

The paper will initially discuss the nonlinear characteristics of airfoils and how this affects the high loads that are seen on a helicopter at the limits of the flight envelope. Three test cases from a UH-60A in flight will be examined to observe both similarities and differences in the effects of dynamic stall on the loads. Initially, dynamic stall will be observed in terms of conditions on the rotor, that is, where does blade stall occur in azimuth and rotor radius. Following the examination of stall in a global sense the remainder of the paper will focus on the details of dynamic stall on the blade sections. A number of conclusions will be offered relative to characteristics of dynamic stall on helicopter rotors.

### Dynamic Stall and Control System Loads

A well-designed rotor will not experience significant dynamic stall in its normal operating envelope. However, in maneuvering flight or under heavily loaded conditions a rotor will reach its thrust limit and dynamic stall will occur causing significantly increased blade torsion and control system loads. As an example, for the UH-60A, the pitch-link loads in severe maneuvers are about 2.5 times greater than the loads in maximum speed level flight (Ref. 6). The cause of these increased loads is related to aerodynamic moments on the blade under stalled conditions. Figure 1 shows  $C_L$  as a function of  $C_M$  for the SC1095 airfoil based on both static and dynamic 2D wind tunnel test data (Refs. 7 and 8). For lift coefficients below  $C_{L_{max}}$  there is very little change in the moment with changes in lift as is typical of helicopter airfoils. The slightly negative moment in this regime results in the negative mean pitch-link loads (compression) seen on this aircraft. For the static data the section moment becomes strongly negative for angles of attack beyond the maximum static lift coefficient. For the dynamic data, however, there is a lift increase or overshoot that is related to dynamic stall on the blade. About a ten percent increase in  $C_{L_{max}}$  can be obtained beyond the static stall angle without severe penalties in section pitching moment and this overshoot regime is sometimes referred to as the "light stall" region (Ref. 9). Beyond this region of light

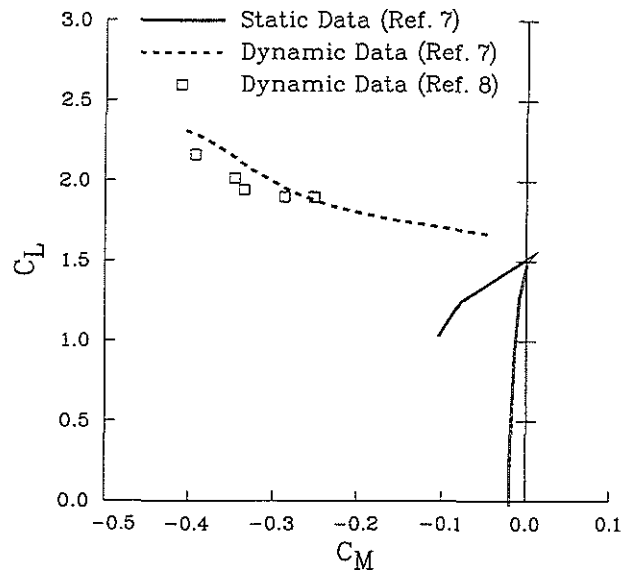


Figure 1. Moment coefficient as a function of lift coefficient for SC1095 airfoil.

stall, large negative pitching moments dominate the problem and any slight improvement in lift performance is paid for in excessive control system loads. Within this region of large negative pitching moments, referred to as the "deep stall" region (Ref. 9), the extensive measurements and visualization that have been obtained from numerous 2D wind tunnel experiments provide a good understanding of the phenomena involved. As the blade angle of attack exceeds the dynamic stall limit one or more vortices are shed from the forward part of the airfoil. These vortices are convected back along the airfoil at a speed somewhat less than the free stream and pass off the trailing edge. "Moment stall" is generally associated with the formation of the dynamic stall vortex while "lift stall" occurs when the dynamic stall vortex leaves the airfoil trailing edge. The dynamic stall process in the light stall region is sensitive to numerous parameters and significant differences are seen between airfoils. Within the deep stall region, however, the dynamic stall behavior shows little difference between airfoils (Ref. 9).

The knowledge obtained on dynamic stall from 2D wind tunnel testing provides a useful basis for understanding dynamic stall on a helicopter rotor in forward flight and maneuvers. However, significant differences exist between the two environments and it is useful to mention some of these differences here. The angle of attack on an airfoil can be expressed as

$$\alpha = \theta_{cont} + \theta_{elas} - \phi$$

In a conventional 2D wind tunnel test, the model is made rigid so that elastic motion, even at the highest frequencies, is one to two orders of magnitude smaller than

the control angle (Ref. 3). Similarly, the induced flow angle is normally small and is neglected. For a helicopter in flight, however, all three of these angles are of approximately the same size. It is possible in flight to measure the control angle of a rotor with reasonable accuracy and, with some care, derive the elastic deformation in the blade from strain-gauge measurements. However, the induced flow angle is dependent upon the shed wake of the blade, the inflow induced by all other blades, and the flow induced by the fuselage. These angles are not easily measured or calculated. Pressure measurements obtained in flight will provide valuable information, particularly as concerns section normal force and pitching moment. However, the lack of an accurate knowledge of the blade angle of attack in flight will be a source of frustration in interpreting the data.

### UH-60A Flight Test

A UH-60A helicopter was extensively instrumented for flight test measurements including the installation of 242 pressure transducers on one blade that are arranged to allow the calculation of section lift, pitching moment, and chord force at nine radial stations. The aircraft, its instrumentation, and the flight test program are described in Ref. 5. Maneuver data obtained during the test program have been examined and ranked in order of the severity of the loading in Ref. 6. The data from two high-torsional load maneuvers, a symmetric pull-up and a high-speed, diving turn, are used here as a basis for an examination of dynamic stall. In addition, a steady flight case at high altitude, near the rotor thrust boundary, is also selected. Figure 2 compares the selected test conditions with a rotor thrust boundary determined from model rotor test data by McHugh (Ref. 10). The y-axis is defined as the product of the vehicle load factor and the weight coefficient,  $n_z * C_W / \sigma$ , to allow a comparison of both steady and maneuvering flight. The first maneuver, a 2.1g UTTAS pull-up (Counter 11029), is shown in Fig. 2 by plotting the mean  $n_z * C_W / \sigma$  for each revolution as a function of the mean advance ratio. The aircraft is able, in this case, to achieve a rotor thrust that is well in excess of the McHugh boundary, which is based on steady rotor performance. The second maneuver is a diving right turn at high speed (Counter 11679) and in this case the load factor is less than for the pull-up, but the airspeed is greater. The aircraft descent rate for this maneuver is about 4000 ft/min and a bank angle of about 55 deg is achieved. Nominally, angular accelerations for this maneuver are zero (unlike the pull-up) although the angular rates are non-zero. The third case is a steady flight condition at  $C_W / \sigma = 0.13$  (Counter 9017). Steady, level flight data were obtained at six values of  $C_W / \sigma$  during the test program, as shown in Fig. 2, and the selected case was the maximum load flight condition obtained. The high loading for this condition was obtained by flying at high altitude to reduce density, rather than by increasing the gross weight. Specific revolutions

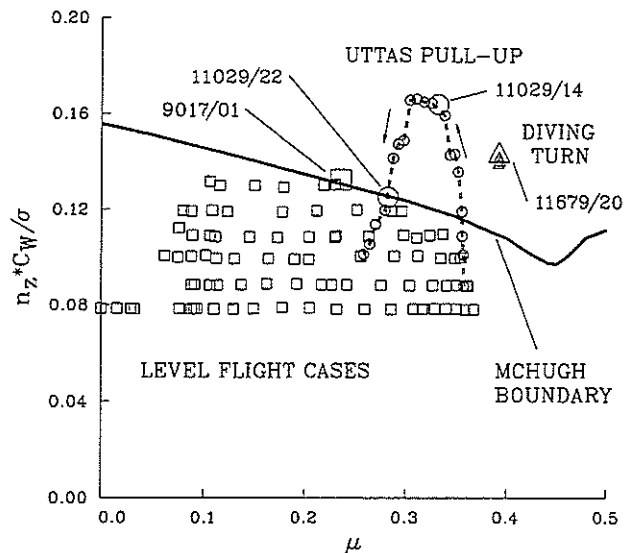


Figure 2.  $n_z * C_W / \sigma$  as a function of advance ratio showing selected test conditions.

examined in detail later in this paper are indicated in Fig. 2 by enlarged symbols.

The oscillatory pitch-link loads (half peak-to-peak) during the UTTAS pull-up are shown in Fig. 3. The initial peak in the loads occurs at about Rev 13 or 14 and the loads remain relatively constant over the next few revolutions, varying from 2500 to 2860 lbs. After Rev 22 the pitch-link loads rapidly decrease. The rotor thrust, represented by  $n_z * C_W / \sigma$ , starts to decrease at about Rev 17, so that by Rev 22 the load factor has dropped from 2.1 g to 1.6 g. Two revolutions, 14 and 22, are selected as representative of the maneuver as the oscillatory pitch-link loads are similar in magnitude, but the advance ratio, load factor, and pitch rate all differ. The UTTAS pull-up represents a fairly severe loading condition for this aircraft. For example, the maximum oscillatory pitch-link loads reported on the UH-60A during air-to-air combat tests were 2700 lbs and the maximum encountered in the flight loads survey during the aircraft development were 3040 lbs (Ref. 11).

## Global Stall Characteristics

### Rotor Disk Stall Maps for Selected Cases

The UH-60A rotor data are first examined for indications of deep stall, specifically for signs that a dynamic stall vortex is being formed and shed. From the normal force time histories at the various radial stations it is possible to identify the presence of lift stall in some

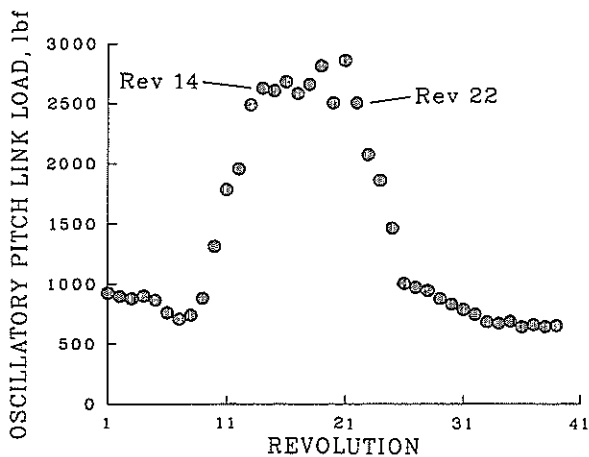


Figure 3. Oscillatory pitch-link loads measured during UTTAS pull-up.

cases and the azimuth associated with this event is one indicator of stall. In a similar manner the pitching moment time histories are examined and the radius and azimuth where moment stall is observed represents a second indicator of stall. Finally, the upper surface pressure time history at 0.963c is examined which shows whether the boundary layer is separated or attached and this represents a third indicator of stall on the disk. Each revolution of data in the maneuver is treated here as a separate event and the thrust, airspeed, pitch rate, and so forth are assumed to be represented by the mean values computed over the one revolution. This quasi-steady assumption is appropriate for the level flight case, but is an approximation for the maneuver cases.

Figure 4 shows the section normal force as a function of blade azimuth for Rev 14 of the UTTAS pull-up. The nondimensional section normal force,  $M^2 C_L$ , is normalized by the speed of sound rather than the local section velocity and, hence, is a global representation of force on the blade. The azimuth range shown is unconventional in that the starting azimuth is 135 deg, half way through the second quadrant of the rotor. This shift in the azimuthal reference is used here as stall on the UH-60A develops near the beginning of the third quadrant and, in some cases extends through the end of the first quadrant. By shifting the data to the 135 deg reference it is possible to study the stall cycles in their entirety. In the plot of normal force in Fig. 4 the data at each radial station are offset by an arbitrary amount so that the behavior of the normal force at each radius can be clearly seen and related to the behavior at adjacent stations.

The rotor data were acquired at a fixed sample rate that is equivalent to an azimuth stepsize of about 0.72 deg. Anti-aliasing filters were used with a frequency cut-off of 550 Hz and this is equivalent to an azimuth stepsize of about 1.42 deg. For this paper the data obtained in the experiment on a time base have been transferred to an

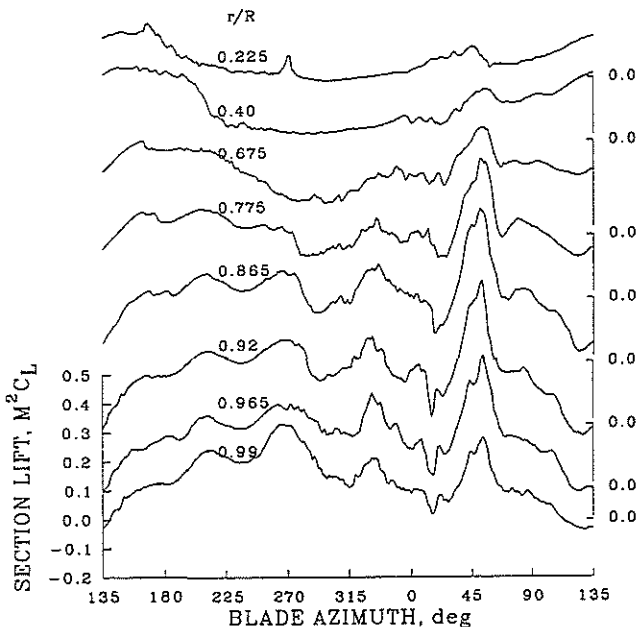


Figure 4. Offset plot of section normal force for UTTAS pull-up; Rev 14.

azimuth base using linear interpolation. The azimuth base selected here uses a stepsize of 1.5 deg and is equivalent to the anti-aliasing filters used. No section data are shown at 0.55R for this counter because of instrumentation failures on the lower surface that prevent an integration of the acceptable pressure measurements.

The normal force time histories in Fig. 4 were examined for cases of lift stall and the associated azimuth was recorded as one indicator of dynamic stall on the blade. Lift stall is most clearly observed in Fig. 4 for the radial stations from 0.775R to 0.92R. Stall is initially seen between 273 and 278 deg. A second peak indicative of lift stall is seen at about 330 deg and is more prominent outboard. At the very beginning of the first quadrant, at about 5 deg, a limited area of lift stall can be seen towards the tip. Finally, in the center of the first quadrant lift stall is observed between 51 and 54 deg and extends from 0.675R to the tip. There is also a suggestion of lift stall at about 170 deg at the most inboard station, 0.225R, and also at about 190 deg at 0.40R although its occurrence is unclear. A short duration pulse at 272 deg at 0.225R is seen just before the reversed flow boundary and this is caused by a disturbance at the rear of the airfoil, mostly at 0.607c. The cause of this disturbance is unknown and it does not occur in other revolutions for this maneuver or in the other maneuvers. Although the azimuth of lift stall is determined to the nearest 1.5 deg, as defined by the resolution of the data, the accuracy of this determination is less. In some cases it is unclear which of two or more features in the time history best indicate lift stall and, in these cases, multiple azimuths are recorded.

The section moments for the UTTAS pull-up, Rev 14, are shown in Fig. 5 in the same offset plot format as in Fig. 4. These time histories were examined to identify

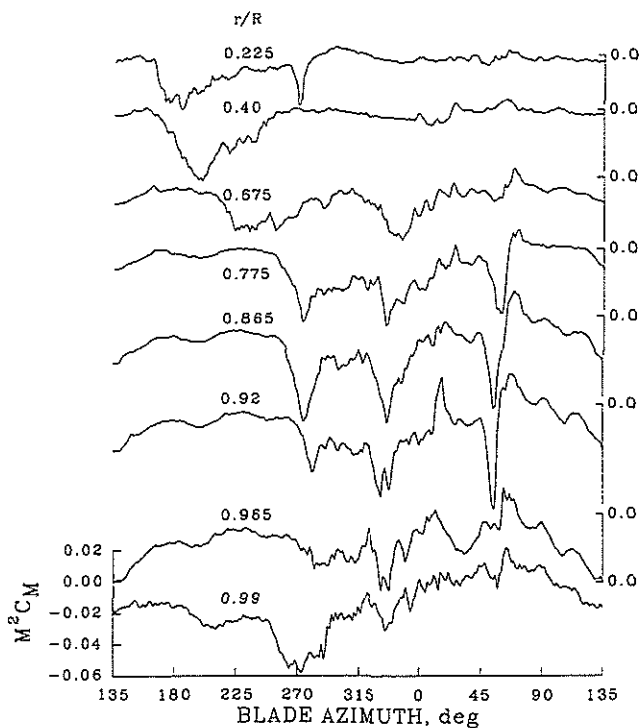


Figure 5. Section pitching moments for UTTAS pull-up; Rev 14.

incidences of moment stall and the azimuths associated with moment stall were recorded. In Fig. 5 moment stall is observed at nearly all of the stations and, where most pronounced, appears similar to traces of moment stall data obtained in 2D wind tunnel tests. Moment stall is observed at the inboard stations, occurring at 164 deg at 0.225R and 166 deg at 0.40R. Outboard, from 0.775R to 0.92R, moment stall associated with a first dynamic stall cycle is seen from 252 to 263 deg. A second stall cycle is apparent from 0.675R to the tip and occurs between 320 and 330 deg. A third cycle, occurring at about 45 deg in the first quadrant causes large moments from 0.775R to 0.92R, but not outboard.

Trailing edge pressure data are shown in Fig. 6 for Rev 14 of the UTTAS pull-up using the offset plot format. Under normal flight conditions the trailing edge pressures show little variation with azimuth except that outboard on the rotor, there is a slight 1/rev variation that peaks in the fourth quadrant. The time histories in this figure, however, all show significant excursions in the pressure that are associated with boundary layer separation and loading by the dynamic stall vortex. These trailing edge pressures were examined to identify these separation events and the associated azimuths were recorded. Inboard, at 0.225R, the flow starts to separate at about 176 deg and then reattaches at about 227 deg. There is a similar area of separation at 0.40R and interestingly, a very small area of separation at about 15 deg that is associated with the second stall cycle. At 0.675R to 0.865R three distinct areas of separated flow are observed and these correspond

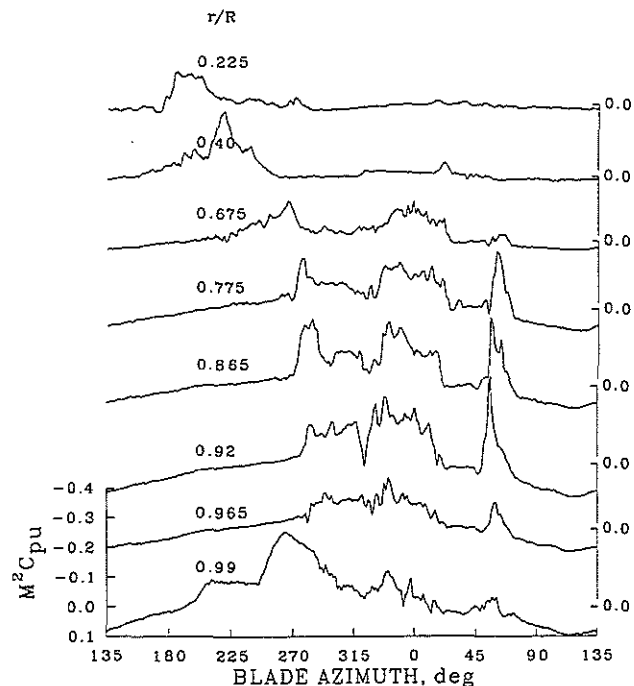


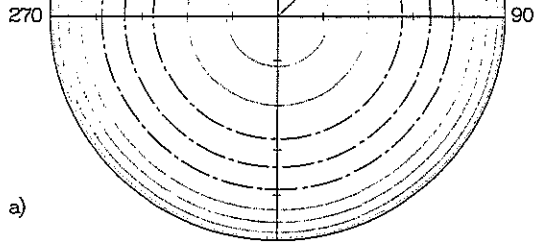
Figure 6. Upper surface trailing edge pressures for UTTAS pull-up; Rev 14.

with the three stall cycles seen in the pitching moment data. At 0.92R it appears that the separated flow associated with the first dynamic stall cycle continues into the second cycle and the boundary layer is never able to reattach. At 0.965R the flow appears to be separated continuously from 282 to 17 deg. At 0.99R, about three in from the blade tip, minor flow separation is observed beyond 315 deg that is associated with dynamic stall, but the greatest effects seen are around 270 deg where a large separation zone forms that is probably related to the tip vortex lifting off the aft portion of the airfoil under these high lift conditions.

The azimuths identified from the qualitative analysis of the time histories of normal force, pitching moment, and trailing edge pressures, as described above, are mapped onto the rotor disk as a means of describing how stall occurs on this rotor. Figure 7 provides such a map of blade stall for the UTTAS pull-up. Rev 06, the entry to the maneuver, is the first map shown and subsequent rotor maps are shown for every other revolution through the maneuver. The rotor maps are oriented in the conventional fashion with the 0 deg azimuth at the rear of the disk and with the wind coming from the front at 180 deg. A reference line is shown at 135 deg as a reminder that the data analysis starts at this azimuth. The circumferential lines on the maps represent the nine measurement stations plus the blade tip at 1.00R. These circumferential lines are shown as dotted lines for the radial stations with the SC1095 airfoil and as chain-dashed lines for sections with the SC1094R8 airfoil. The SC1094R8 is a modification of the SC1095 with added camber and droop at the nose and is used over the center span of the blade. Moment

Rev 06  
 $\mu = 0.358$   
 $n_z = 1.11$

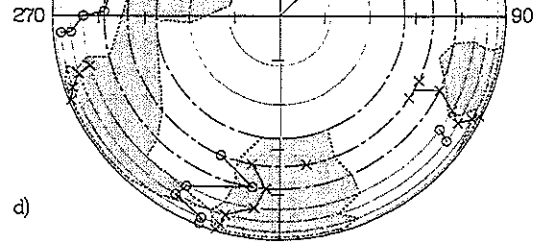
$q = 14 \text{ deg/sec}$   
 $P/L_{osc} = 762 \text{ lbs}$



a)

Rev 12  
 $\mu = 0.350$   
 $n_z = 1.95$

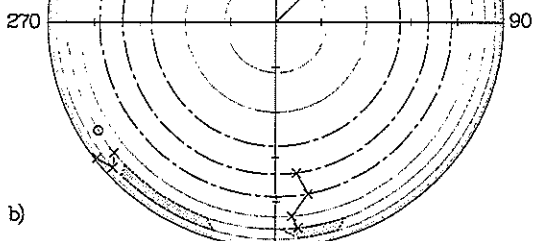
$q = 14.5 \text{ deg/sec}$   
 $P/L_{osc} = 1959 \text{ lbs}$



d)

Rev 08  
 $\mu = 0.358$   
 $n_z = 1.43$

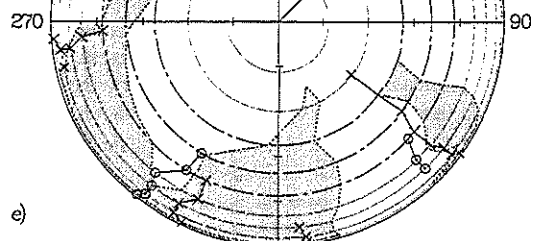
$q = 9.6 \text{ deg/sec}$   
 $P/L_{osc} = 741 \text{ lbs}$



b)

Rev 14  
 $\mu = 0.341$   
 $n_z = 2.09$

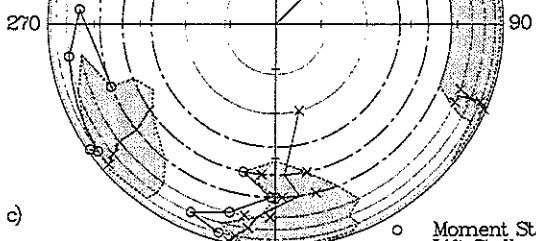
$q = 14.2 \text{ deg/sec}$   
 $P/L_{osc} = 2631 \text{ lbs}$



e)

Rev 10  
 $\mu = 0.357$   
 $n_z = 1.75$

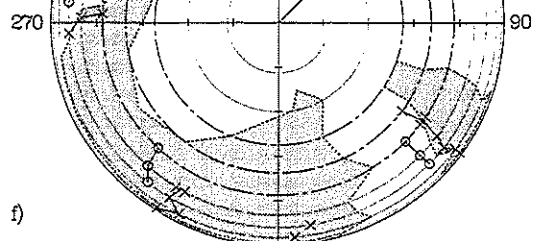
$q = 13.1 \text{ deg/sec}$   
 $P/L_{osc} = 1316 \text{ lbs}$



c)

Rev 16  
 $\mu = 0.329$   
 $n_z = 2.11$

$q = 12.9 \text{ deg/sec}$   
 $P/L_{osc} = 2685 \text{ lbs}$



f)

o Moment Stall  
 x Lift Stall  
 [shaded] Separated Flow

Figure 7. Dynamic stall rotor map for UTTAS pull-up – continued.

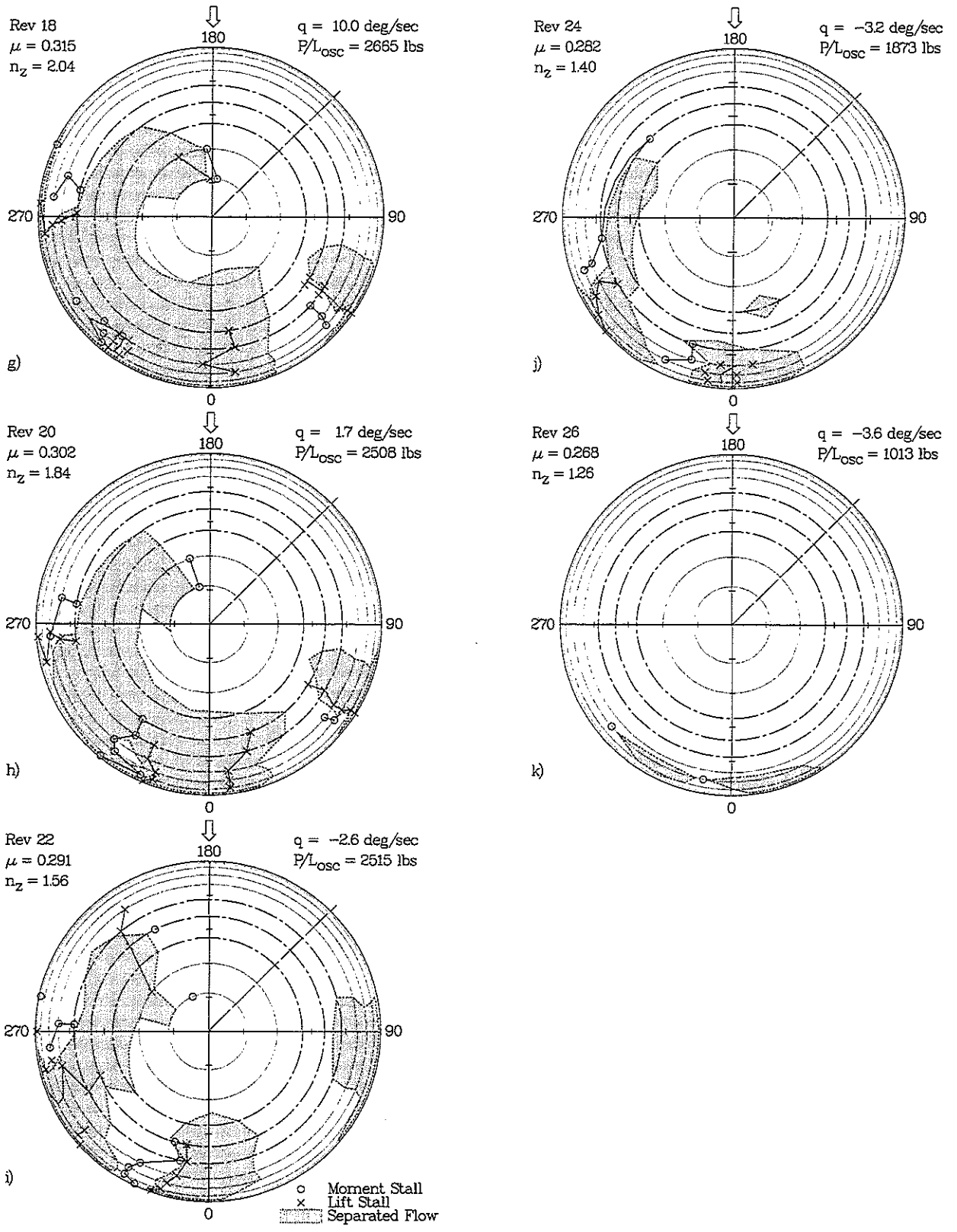


Figure 7. - concluded.

stall azimuths are shown with an open circle and, where appropriate, a line connects adjacent stations. The lift stall azimuth locations are indicated with an "x" in a similar fashion. Separated flow is shown with a dotted boundary and the portion of the disk where the flow is separated is shown as a gray or stippled area. Adjacent to each rotor map are the mean values of the advance ratio, load factor, pitch rate, and oscillatory pitch-link load during the single revolution that is mapped. The section forces and moments could not be obtained for the 0.55R station because of failed instrumentation on the lower surface. Moreover, the upper surface pressure transducer at 0.963c at 0.55R also failed but it was possible to use the lower surface transducer at 0.963c to indicate regions of separated flow. Thus the maps include markers for separation at this station but none for lift or moment stall.

Rev 06, Fig. 7a, is essentially the starting point of the maneuver with  $\mu = 0.358$ , the load factor just above one g, and the pitch rate nominally zero. There is no indication of stall anywhere on the rotor disk. As the pitch rate becomes positive and the load factor increases in Rev 08, there are signs of moment stall just past 180 deg for the two inboard stations and two patches of separated flow are observed at the aft edge of the disk towards the tip of the blade. There are indications of lift stall associated with both patches although moment stall was detected only prior to the first patch. For Rev 10, the airspeed has not begun to bleed off, while both the load factor and pitch rate continue to increase. Four patches of separated flow are observed for this revolution, three outboard on the blade and mostly towards the rear of the disk and one patch inboard on the blade just to the left of the nose of the aircraft. It seems clear that this inboard patch is related to an increase in the local angle of attack that is induced by aerodynamic flow over the nose of the aircraft. At Rev 06 the aircraft pitch attitude is minus four or five deg, but as the nose is pitched up, the fuselage angle of attack becomes positive. For Rev 10, the aircraft pitch attitude is about plus six deg and rapidly increasing. The first two stall cycles for Rev 10 give clear indications of both lift and moment stall, while the third cycle only shows indications of lift stall. Clear, unambiguous signs of lift stall or moment stall are not always obvious in the normal force and pitching moment data and, in these cases, no marker is placed on the rotor map. In other cases, there may be an obvious indication of lift or moment stall, but some ambiguity in the azimuth at which it occurs. In some cases two or more markers are used to indicate a stall event, for instance, in Rev 10 for the lift stall in the second cycle. The use of multiple markers is an indication of uncertainty in identifying the azimuth of lift stall in the original normal force plot. The maximum pitching rate is reached in Rev 12, although the load factor is still below its maximum and the alternating loads are only about 70% of the maximum observed in the maneuver. The stall on the inboard blade stations that occurs over the nose of the aircraft is now connected in a continuous fashion with the first stall cycle on the outer part of the blade. Because the radial location of stall for this first cycle is such a strong

function of azimuth, stall is only occurring over a limited portion of the blade at any one time. There is some indication outboard at 0.92R that the flow is not completely reattaching before the second stall cycle begins. However, full reattachment is achieved prior to the third stall cycle in the first quadrant.

Rev 14 is the first of the revs at the top of the high pitch-link load conditions indicated in Fig. 3. The advance ratio is still above 0.34, the load factor is about 2.1 g, and the pitch rate remains near its maximum. The first dynamic stall cycle appears to be continuous from the most inboard station, where it occurs over the nose of the aircraft at about 170 deg to the blade tip where moment stall starts just before the 270 deg azimuth. Outboard of 0.865R the boundary layer never reattaches between the first and second stall cycles but remains separated for a full quadrant. Near the end of the second stall cycle outboard there are indications of lift stall, even though the flow has not reattached (see also Fig. 4). At the beginning of the first quadrant the boundary layer reattaches along the entire blade and then, at about 45 deg, stall occurs simultaneously from 0.55R to the tip.

Although the airspeed is reduced in Rev 16 the load factor and oscillatory pitch-link loads remain at their peak. The area of separated flow that connects the first two stall cycles now extends inboard of 0.775R. Even though the flow is fully separated there are clear indications of moment stall in the section moment data from 0.775R to 0.92R. By Rev 18 the advance ratio has decreased to 0.315, but the load factor is still in excess of two. The separated flow region that connects the first two cycles now extends inboard of 0.55R. At this point in the maneuver, over a quarter of the rotor disk is fully separated. The third stall cycle, at the end of the first quadrant on the advancing side, still remains distinct from the first two cycles. Rev 20 shows significant areas of separation connecting the first two stall cycles as was seen in Rev 18. Note, however, that there is a small patch of reattached flow that occurs at 0.865R and 0.92R between the first and second cycles. The third stall cycle appears much as before, based on this qualitative map, but the amplitudes of the moments for the third cycle are significantly reduced in Rev 20 from Rev 18.

The mean advance ratio has dropped to 0.291 by Rev 22 and the mean load factor to 1.56. Interestingly, the alternating pitch-link loads still exceed 2500 lbs while the pitch rate is now slightly negative. There is some indication of stall in the first half of the third quadrant, but it is not clear how this is related to the stall cycle that starts just prior to 270 deg at the outboard stations. The flow reattaches after this cycle and a new stall cycle starts again at about 330 deg. The third stall cycle, in the last part of the first quadrant, that had been prominent in previous revolutions is largely gone. There is no clear indication of lift or moment stall and the separated flow mapped here may be more directly related to shock-boundary layer separation than dynamic stall. As the aircraft recovers in the maneuver the loads decline rapidly as the number and extent of the stall cycles decline. In

Rev 24 two stall cycles remain, but the areas of separated flow have lessened. Finally, in Rev 26, moment stall is observed only at two azimuths for 0.92R and only a small area of separated flow is associated with each patch.

The examination of stall growth and decay during the UTTAS pull-up is valuable for the perspective it provides on the development of stall on the rotor disk during limiting flight conditions. However, it is not immediately apparent how much of the stall characteristics observed are dependent upon unsteadiness in the aircraft state during the maneuver and how much is directly associated with the basic stall characteristics of the airfoil and the elasticity of the blade and controls. The second maneuver of interest for this paper is a high-speed, diving turn and, nominally, all angular accelerations are zero and the only difference from a steady case are the non-zero angular rotations that are associated with the steady turn. As a practical matter, obtaining steady conditions in a diving turn is a difficult piloting task, but it appears that at least four contiguous revolutions near the peak load factor obtained for this maneuver are repeatable (Ref. 12). One revolution from this maneuver has been examined, Rev 20, using the same qualitative approach as described for the UTTAS pull-up. Figure 8 shows the rotor map for this case and although the advance ratio, 0.39, is higher than in the UTTAS pull-up, the load factor is less. The oscillatory pitch-link loads of 2600 lbs are comparable to the most severe loading in the UTTAS pull-up. Comparison of this figure with Rev 14 of the pull-up, Fig. 7e, shows some similarities, particularly in the distribution of the first and third stall cycles and the extent of the separated flows. However, what is lacking in Fig. 8 is an indication of a second stall

cycle beginning near 330 deg. Outboard on the blade there appears to be a limited area of lift stall and, perhaps, a bit of moment stall at 0.675R, but there is no clear indication of a new stall cycle starting at the middle or end of the fourth quadrant. The differences with, for instance, Rev 14 or Rev 22 of the UTTAS pull-up remain as interesting as do the similarities.

The third test condition examined is the maximum level flight loading case obtained in the flight test program. This level flight condition was flown just under 17,000 ft to obtain a high thrust coefficient by using decreased density instead of increased weight. As shown in Fig. 2, the  $C_W/\sigma$  of 0.13 is at the steady thrust boundary as determined by McHugh. The rotor map for this condition is shown in Fig. 9 and two stall cycles can be seen in much the same positions as observed in Figs. 7 and 8. Note, however, there is no indication of a third stall cycle in the first quadrant of the rotor. As is expected for a level flight condition, the pitch attitude of the aircraft is nose down and little effect of fuselage induced flow should be seen inboard on the rotor and that is, in fact, the case as there is no suggestion of stall over the aircraft nose. The first stall cycle is seen to start midway through the third quadrant and then move outboard towards the blade tip where moment stall is seen at about 280 deg at 0.965R. The flow reattaches and then a second cycle occurs towards the end of the fourth quadrant. This steady case shows strong similarities with both the UTTAS pull-up and the diving turn in terms of the stall map. Note, however, that the oscillatory pitch-link loads are much lower. This is a result, in part, of the low density at the flight altitude for this condition.

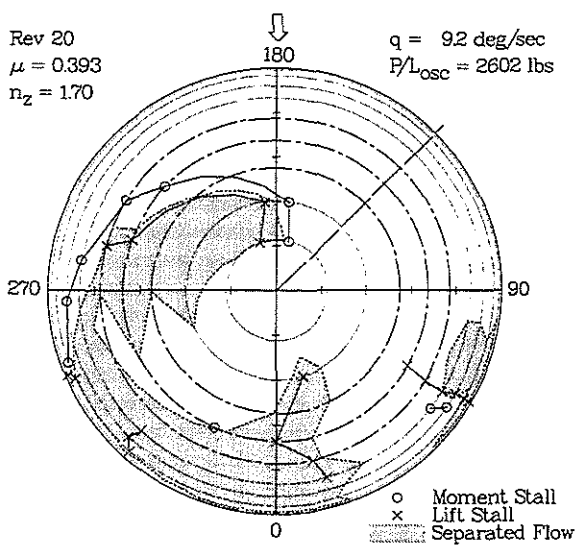


Figure 8. Dynamic stall rotor map for high-speed, diving turn; Rev 20.

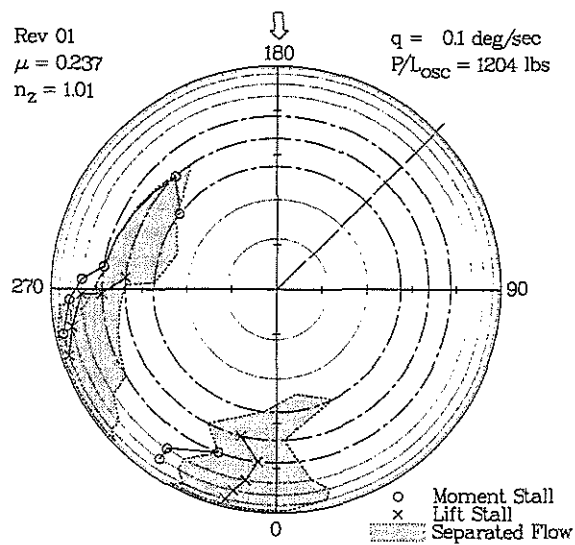


Figure 9. Dynamic stall rotor map for steady, level flight; Rev 01.

## Discussion of Global Stall Characteristics

An examination of the rotor stall maps for the cases shown here suggests that the qualitative indicators of stall, that is, lift stall, moment stall, and trailing edge separated flow, all provide considerable insight into the stall characteristics of this aircraft. The wealth of experimental results from 2D wind tunnel testing shows that deep stall is characterized by the formation of a dynamic stall vortex over the forward part of the airfoil and that moment stall is related directly to this vortex formation. As the stall vortex moves over the upper surface of the airfoil the pitching moment becomes more negative but the lift is maintained and lift stall does not occur until the dynamic stall vortex leaves the airfoil's trailing edge. Lift stall, then, lags moment stall by the time it takes for the vortex to pass over the airfoil. Large separated flows occur at the trailing edge when the vortex leaves the trailing edge. The rotor maps show these characteristics, for the most part, indicating that knowledge based on 2D wind tunnel testing is of value in understanding the stall shown here on the rotor disk.

The stall maps also provide qualitative information on the three-dimensional characteristics of dynamic stall on a flight vehicle. Except for the area of stall inboard on the blade that occurs over the nose of the aircraft because of fuselage-induced flows, stall is largely an outboard phenomenon on this rotor. Stall and the formation of the dynamic stall vortex are observed right to the blade tip, unlike the wind tunnel tests of an oscillating wing reported in Ref. 3 where the dynamic stall vortex was not observed within two chord lengths of the tip (about 0.865R for this rotor). The formation and shedding of the dynamic stall vortex appears quite two-dimensional in the third stall cycle (in the first quadrant) and referring to Fig. 7e or 7f it is easy to visualize a continuous dynamic stall vortex forming at about 45 deg, and then moving rearwards on the airfoil as a single, continuous structure from 0.40R to the tip. However, for the initial stall cycle that is observed in the third quadrant, the dynamic stall vortex is quite three-dimensional in the sense that while it is leaving the trailing edge at 260 deg at 0.675R, for example, it has not yet formed outboard at 0.775R. It seems likely that the dynamic stall vortex for this initial cycle is also a single, continuous structure, but that it is formed and shed over a broad azimuth range and its passage over the blade at any radius occurs only over a narrow azimuth range.

Another feature of the stall maps that is striking is the regularity of the stall patches. This is particularly apparent comparing the three different flight cases. The actual blade angle of attack is unknown for these conditions, as discussed earlier, but the pattern is obviously the consequence of the angle-of-attack variation along the blade and around the azimuth. The stall patches occur at about a frequency of 4/rev or 5/rev and as the control angle,  $\theta_{cont}$ , has only first harmonic variation it cannot explain the higher frequency cycles seen here. The inflow angle may well vary at higher frequencies, but the

regularity of this pattern over all flight conditions strongly suggests that the torsional deflection in the blade,  $\theta_{elas}$ , which is a result of both blade and control system flexibility, is the cause of this repeated pattern.

The qualitative similarities of the stall maps for the three test conditions are quite interesting, but it is also important to note differences in these maps for conditions that result in high oscillatory pitch-link loads. A comparison of Revs 14 and 22 from Fig. 7 and Rev 20 from Fig. 8 show a number of differences even though each of these cases shows approximately the same oscillatory loads. Rev 14, from Fig. 7, shows a dynamic stall vortex shed prior to each of the three stall cycles. Rev 22, on the other hand, shows a dynamic stall vortex for the first two cycles, but not the third, while Rev 20 from Fig. 8, shows an extended dynamic stall vortex for the first cycle, a smaller vortex for the third, and essentially none for the second cycle. While the pattern of these stall maps is controlled by the torsional dynamics, the actual angles of attack and the resulting loads are a consequence of the many factors affecting the induced flow.

## Dynamic Stall on the Blade

### Blade Surface Pressures

The blade upper surface pressures are shown in Fig. 10a as a function of rotor azimuth for the 0.865R station for Rev 14 of the UTTAS pull-up. The offset format is used with the initial azimuth at 135 deg and the time histories of the individual pressure transducers are ordered from leading edge to trailing edge. The formation of a dynamic stall vortex at the front of the airfoil and its convection along the airfoil and off the trailing edge is made apparent in this figure by the offset of the individual transducers. The initial formation of the vortex occurs at about 260 deg and passes the trailing edge at about 275 or 280 deg. The flow remains largely separated on the upper surface and a second cycle starts at about 310 or 315 deg. This second dynamic stall vortex is more difficult to distinguish than the first, perhaps, and it appears to leave the trailing edge at about 335 or 340 deg. Just past zero deg, at the start of the first quadrant the first three pressure transducers show a significant drop and there is a loss in lift associated with this pressure drop. However, this loss in lift does not appear to be associated with the formation of a dynamic stall vortex. At about 45 deg the blade stalls again and a third dynamic stall vortex is shed from the blade.

Other features of the flow that are observed in Fig. 10a include the passage of shocks over individual pressure transducers. To better identify the locations of shocks and regions of supercritical flow on the airfoil surface the sonic point has been computed for each pressure transducer and this is shown in the figure as an open circle. As an example, at 135 deg, the flow is supercritical at 0.320c but subcritical at the next station at 0.395c and a shock is located between the two stations. As the blade advances

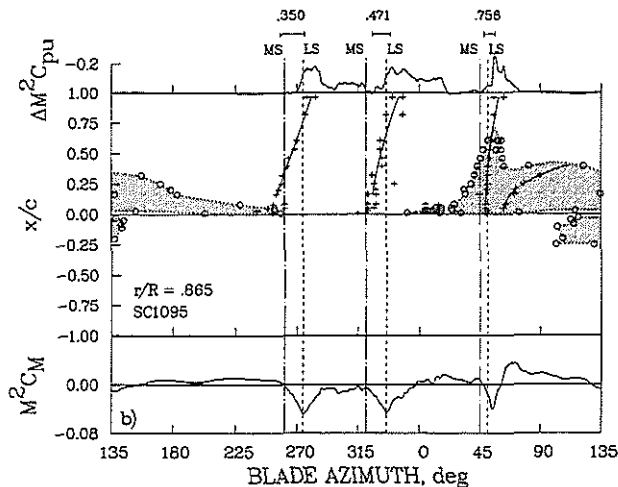
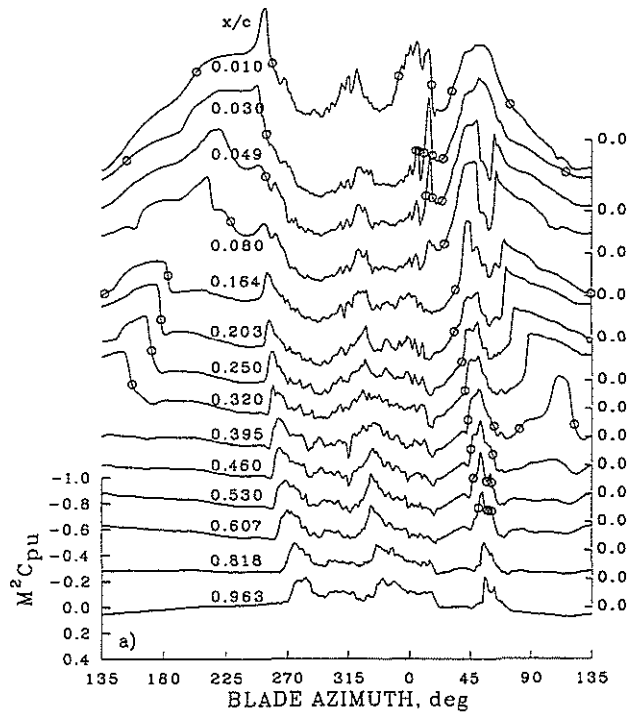


Figure 10. Upper surface blade pressures and airfoil map at 0.865R for UTTAS pull-up; Rev 14.

the shock moves forward on the airfoil and passes over 0.320c at about 155 deg and its passage forward on the airfoil can be followed using the sonic points until finally it reaches the leading edge just as the first dynamic stall vortex is formed. In the first quadrant, the flow on the upper surface is supersonic over most of the front of the airfoil and this leads to a curious "trough-like" appearance at the point of formation of the dynamic stall vortex during the third stall cycle. The flow is supersonic from the leading edge back to about 0.320c, and as the dynamic stall vortex is formed there appears to be a drop in the suction associated with the vortex even though the flow is still completely supersonic. This trough widens in azimuth progressively from 0.049c to 0.320c, and it is not

until 0.395c that the reduction in velocity is sufficient to cause the flow to be subcritical. At the same time the pressure peak that is associated with the dynamic stall vortex remains supercritical until rearward of 0.607c. This dynamic stall event appears complicated by the high local Mach number and the interaction of the dynamic stall vortex, shocks, and supercritical flows.

### Airfoil Maps

Features in the pressure signatures shown in Fig. 10a can be mapped onto a representation of the airfoil surface as shown in Fig. 10b. The central rectangular portion of the Fig. 10b graphic represents both the upper and lower surfaces of the airfoil, unfolded so that the upper portion is the upper surface with the trailing edge as the top boundary and the lower portion is the lower surface with the trailing edge as the bottom boundary. The center line of the rectangle, at  $x/c = 0.0$ , is the leading edge of the airfoil. The x-axis is blade azimuth so the graphic is a representation of airfoil surface events as a function of azimuth and, as before, the initial azimuth is 135 deg. so the full sequence of dynamic stall cycles can be observed.

The azimuths associated with various peaks in the pressure time histories of Fig. 10a can be identified and, knowing the appropriate chord locations these peaks are mapped onto the airfoil surface in Fig. 10b using a "+". In some cases the peaks are readily identified, for example, for the first dynamic stall cycle in Fig. 10a. In other cases there are ambiguities in identifying the actual peaks and subjective judgment is needed, generally by selecting the two or three highest peaks and mapping all of these onto the airfoil surface. The trough that is seen in the first quadrant (third stall cycle) of Fig. 10a is to some extent outlined by the dynamic stall vortex peak on the upstream side and a maximum associated with the pressure recovery on the downstream side. Both the upstream and downstream peaks are mapped in Fig. 10b as a means of visualizing the trough-like structure.

The convection of the dynamic stall vortex in the first stall cycle is fairly well marked by the pressure peaks in Fig. 10a and the vortex passage is emphasized on the airfoil surface of Fig. 10b by fitting a second-order polynomial which is included in the figure. A polynomial is also used to fit the peaks for subsequent dynamic stall cycles as well as the boundary on the downstream side of the trough associated with the third dynamic stall cycle.

The sonic points identified in Fig. 10a can also be mapped onto Fig. 10b as a means of defining the boundaries of supercritical flow regions on the airfoil surface. The mapped sonic points are shown in Fig. 10b with the same open circle symbol used in Fig. 10a. These points are then connected and the supercritical flow regions are shown as a stippled area in the manner of Ref. 13. On the upper surface the flow becomes supercritical at the leading edge at about 0 deg. and, then, in the first quadrant, the supercritical flow region extends back on the airfoil as the local Mach number increases. If the supercritical flow region depended only upon Mach number then it would be

a maximum at about 90 deg., but the blade angle of attack is being reduced in the first quadrant. These two effects, Mach number and angle of attack, work against each other to define the supercritical flow region. At the end of the second quadrant the angle of attack is once again increasing, but the Mach number is decreasing and the supercritical flow region moves forward until it disappears as the first dynamic stall vortex is formed. Sonic points have also been determined on the lower surface of the airfoil, but no attempt has been made to map pressure peaks on that surface. When lower surface peaks occur they are usually substantially smaller than the upper surface ones.

Along the bottom of the Fig. 10b graphic is a plot of the section pitching moment and this clearly shows the moment stall. The moment stall is shown across the entire graphic with a chain-dot line and is labeled with "MS" at the top of the graphic. Although a plot of lift is not included here, the lift stall azimuth previously used for the rotor disk maps is shown with a dashed line and is labeled "LS." Along the top of the graphic is a modified form of the trailing edge pressure. An estimate has been made of the trailing edge pressure in the absence of stall and this unstalled pressure time history has been subtracted from the measured trailing edge pressures to provide the modified pressure shown in the graphic. This method of presentation emphasizes dynamic stall and other flow disturbances at the trailing edge and eliminates the normal 1/rev variation.

The last features included in the Fig. 10b graphic are calculations based on the position of the dynamic stall vortex. The azimuth where the dynamic stall vortex crosses the 50% chord point, calculated from the polynomial fit mentioned earlier, is used to represent the location of the dynamic stall vortex. This azimuth,  $\psi_{0.5c}$ , is used to compute the onset Mach number, which is printed at the top of the graphic, and it is also used to calculate the azimuth range expected for a dynamic stall vortex to pass the entire length of the airfoil if it was convected at 40% of the free stream velocity, a rate based on extensive 2D wind tunnel testing. This azimuth range is shown as a bar immediately below the onset Mach number.

*Airfoil Map for UTTAS Pull-up, Rev 14.* Figure 11 maps characteristics of the blade surface pressures for six radial stations for the UTTAS pull-up, Rev 14. At the most inboard station shown, 0.675R, supercritical flows are seen on the advancing side of the disk. The airfoil at this station is the SC1094R8. The first stall cycle starts at about 205 deg and it appears that the dynamic stall vortex is convected at a much slower rate than would be expected from 2D wind tunnel tests. This result is atypical of most of the dynamic stall events observed in this paper. The formation of two more dynamic stall vortices is observed but both the section moment and the trailing edge pressure suggest that the last of these, the one in the first quadrant, is quite weak. Outboard, at 0.775R,

where the airfoil section is the same as at 0.675R, the extent of the supercritical flow is increased and the first of three dynamic stall vortices is formed as the supercritical flow shrinks to a small area at the leading edge of the airfoil. The flow appears to reattach at about 315 deg and the second dynamic stall cycle is initiated a few degrees later. Supercritical flow develops over the forward part of the airfoil in the first quadrant and the flow again reattaches before the third stall cycle occurs. At this station both the section pitching moment and the trailing edge pressure indicate that the three stall cycles are roughly equivalent in their influence on torsional loading.

The airfoil section transition from the SC1094R8 to the SC1095 occurs between the 0.775R and 0.865R measurement stations. At 0.865R, as seen in Fig. 11c, the extent of the supercritical flow has increased slightly on the upper surface and, for the first time, supercritical flow appears on the lower surface as well. The behavior of the three dynamic stall cycles at 0.865R is similar to 0.775R and, again, the strength of the three dynamic stall vortices appears similar based on the pitching moment and the trailing edge pressure. However, at this station the area of boundary layer reattachment is very small or nonexistent between the first and second dynamic stall cycles.

At 0.92R, just before the swept tip section begins, the supercritical flow at the leading edge of the airfoil extends to 270 deg. and ceases as the first dynamic stall vortex forms. The flow never reattaches prior to the formation of the second dynamic stall vortex and, interestingly, just before the vortex for the second cycle is formed a small patch of supercritical flow forms over the leading edge of the airfoil. The third dynamic stall vortex forms at about 45 deg and the supercritical flow associated with this vortex extends all the way back to the trailing edge. This third stall cycle happens extremely quickly. Based on a convection velocity of 40% of the free stream, the vortex will take only seven and a half deg to go from the leading edge to the trailing edge, which represents only five samples of the time history. The actual interaction of the dynamic stall vortex with the extensive supercritical flow at this onset Mach number of 0.79 is unclear and the phenomena may be more complicated than would be indicated from 2D wind tunnel testing at lower Mach numbers. The pitching moment caused by this third dynamic stall vortex is greater than the moments caused by the first two vortices. At 0.965R three dynamic stall vortices are again observed although both the section pitching moment and the trailing edge pressure indicate that the influence of these vortices is reduced from inboard on the blade. Near the blade tip, at 0.99R, there are still signs of the three dynamic stall vortices that were seen inboard. However, at this station the trailing edge pressure appears to be most strongly affected by the separated flow created when the tip vortex appears to lift off the rear of the airfoil and, locally, the largest moments observed are caused by this factor which has little to do with dynamic stall.

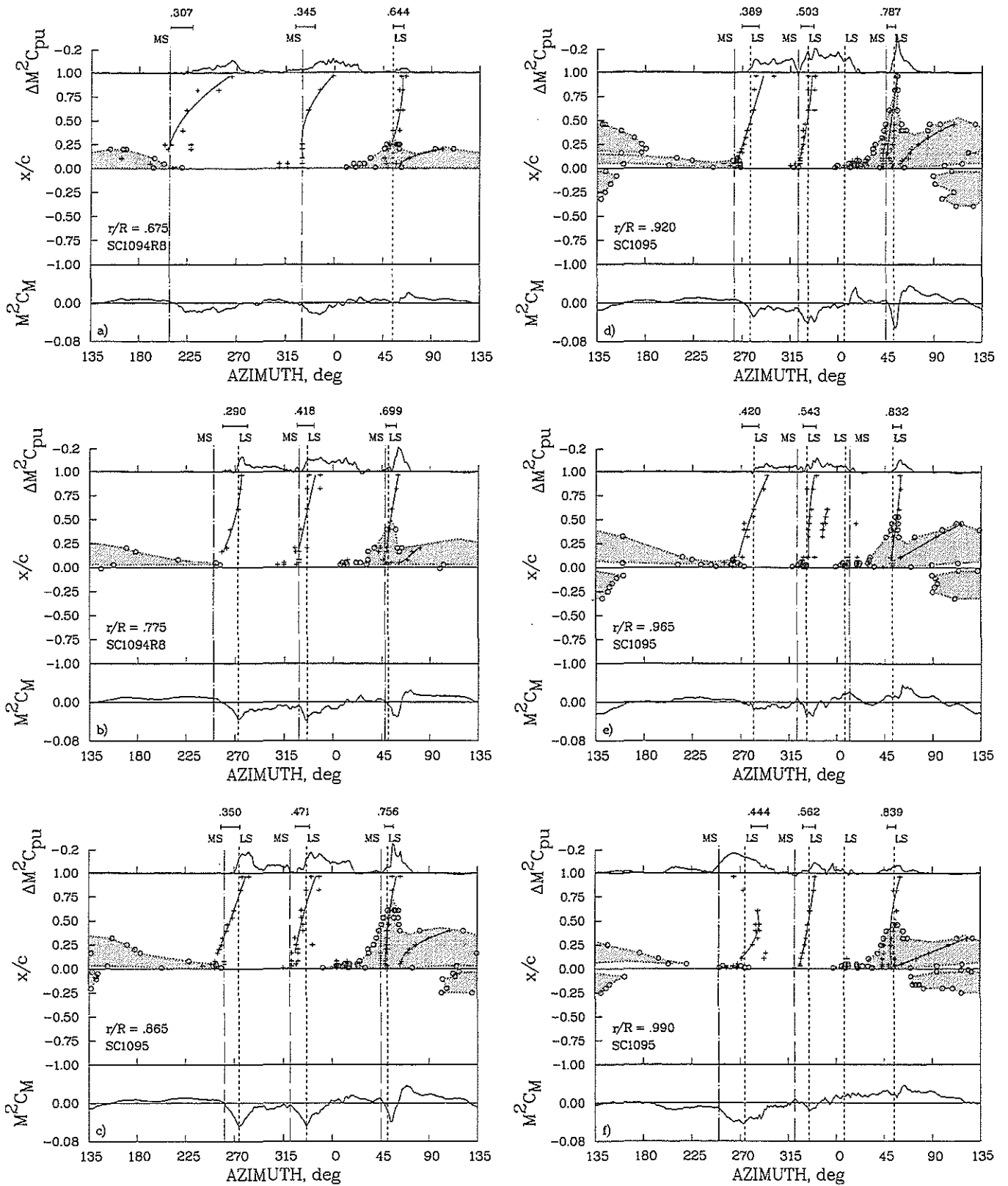


Figure 11. Airfoil map for UTTAS pull-up; Rev 14.

*Airfoil Map for UTTAS Pull-up, Rev 22.* The airfoil maps for the six outboard stations are shown in Fig. 12 for Rev 22 of the UTTAS pull-up. Referring back to Fig. 3 and Fig. 7i, this revolution is the last of the high pitch-link load cycles in the maneuver. Although the oscillatory pitch-link loads remain high for this revolution, the advance ratio, compared to Rev 14, has dropped from 0.34 to 0.29 and the load factor from 2.1 g to 1.6 g. At 0.675R there is less supercritical flow on the airfoil than was seen for Rev 14 and only two dynamic stall vortices appear. Unlike the Rev 14 case, the calculated passage time for the first dynamic stall vortex is a good match of the measurements. At 0.775R a third dynamic stall vortex appears, but the initial vortex appears quite weak while the second and third show moments in excess of what was observed for Rev 14 at this station. There is an area of supercritical flow in the first quadrant and some weak separation on the trailing edge. However, there is no indication of dynamic stall at this location and the separation may be caused by shock boundary layer interaction rather than dynamic stall. At 0.865R, the initial or first dynamic stall vortex seen at about 220 deg is greatly weakened and does not extend aft on the airfoil. The second and third dynamic stall vortices are quite strong, particularly the third one. A fourth dynamic stall vortex now appears on the advancing side, as was seen for Rev 14, but it is quite weak and there is no indication that it affects the pitching moment.

At 0.92R for Rev 22 of the UTTAS pull-up, Fig. 12d, three dynamic stall vortices are seen. The first two, especially the second, show large pitching moments, but the third one on the advancing side is weak and has little effect on the loading. Only two dynamic stall vortices appear at 0.965R and the first one is quite weak. The second, however shows quite large negative moments and areas of separated flow. At the most outboard station, two dynamic stall vortices remain. The first one is quite weak and the moments associated with it are caused by the effects of tip vortex separation rather than dynamic stall. The second dynamic stall vortex is still quite strong even at this station near the blade tip, indicating that the dynamic stall vortex may extend right to the blade tip. In between these two dynamic stall vortices are indications of a much weaker, secondary vortex, and this has been observed in a number of cases in this study. Separated flow is also observed in two other azimuthal locations and may be associated with supercritical flows near the front of the airfoil.

*Airfoil Map for High-speed, Diving Turn.* The airfoil maps for Rev 20 of the high-speed, diving turn are examined in Fig. 13. The loading for this condition is noticeably different from Revs 14 and 22 of the UTTAS pull-up. The advance ratio for this case is 0.39 and the load factor is 1.7g. The oscillatory pitch-link loads are the same as for Revs 14 and 22 of the pull-up, indicating that this condition is equally severe. At 0.675R two dynamic stall vortices are apparent with the second one somewhat stronger based on the pitching moment and trailing edge

pressure. The moments at this inboard station are greater than were seen for either of the pull-up conditions examined. At 0.775R the flow behavior is quite different from Revs 14 and 22 of the pull-up, Figs. 11b and 12b. An initial stall vortex is seen at about 220 deg, but the next two vortices previously observed for this station are absent. Moreover, the flow at this station is separated over most of the azimuth range where the vortices occurred in the pull-up. A weak dynamic stall vortex appears in the first quadrant, but has little effect on the loading. This absence of dynamic stall vortices is also observed further outboard at 0.865R where a number of disturbances are seen on the airfoil surface and the flow is separated from about 270 to 30 deg, but there is no clear indication of dynamic stall. However, a full dynamic stall vortex now appears in the first quadrant on the advancing side.

The reduction in the number of dynamic stall vortices for the diving turn compared to the pull-up is also observed at 0.92R and 0.965R. A vortex forms at about 270 deg at both of these stations and the resulting pitching moments are similar to those seen in the pull-up for this vortex. However, a second dynamic stall vortex that appeared at about 325 deg for the pull-up and was a dominant source of the torsional loading is largely absent from this case. Nonetheless, the separated flows in this region appear greater and more extensive than were observed for the pull-up cases. A dynamic stall vortex is observed in the first quadrant and this vortex provides loading comparable to what was observed for Rev 14 of the UTTAS pull-up. At 0.99R, near the blade tip, the flow on the upper surface is supercritical over the front of the airfoil at all azimuths. Although the loading caused by flow separation induced by the blade's tip vortex is similar to what was seen for the pull-up cases, the associated dynamic stall vortices appear weaker.

*Airfoil Map for Level Flight.* Figure 14 shows the airfoil maps for the six outer stations for the level flight case. The moments at all stations are lower than observed for the maneuver conditions and this is expected as the density for this case is about 65% of the density for the maneuver flying. At 0.675R, two dynamic stall vortices are seen, the first one, at about 225 deg being stronger than the second. A secondary vortex also appears to be associated with this first dynamic stall event. The second dynamic stall cycle is quite weak at this radial station. At 0.775R two dynamic stall cycles are seen as well and, considering the reduced air density, both indicate that fairly strong dynamic stall vortices are being shed. The dynamic stall vortex loading at 0.865R is quite substantial and these two stall vortices appear in the same location as observed for the UTTAS pull-up. A pressure disturbance on the advancing side, at about 80 deg. is suggestive of light stall, but does not extend to the trailing edge.

The outboard stations, from 0.92R to 0.99R show supercritical flow over the upper surface of the blade at nearly all azimuths. Two dynamic stall vortices are observed at each of these stations, and the pitching moment at 0.92R is fairly substantial. As with the other

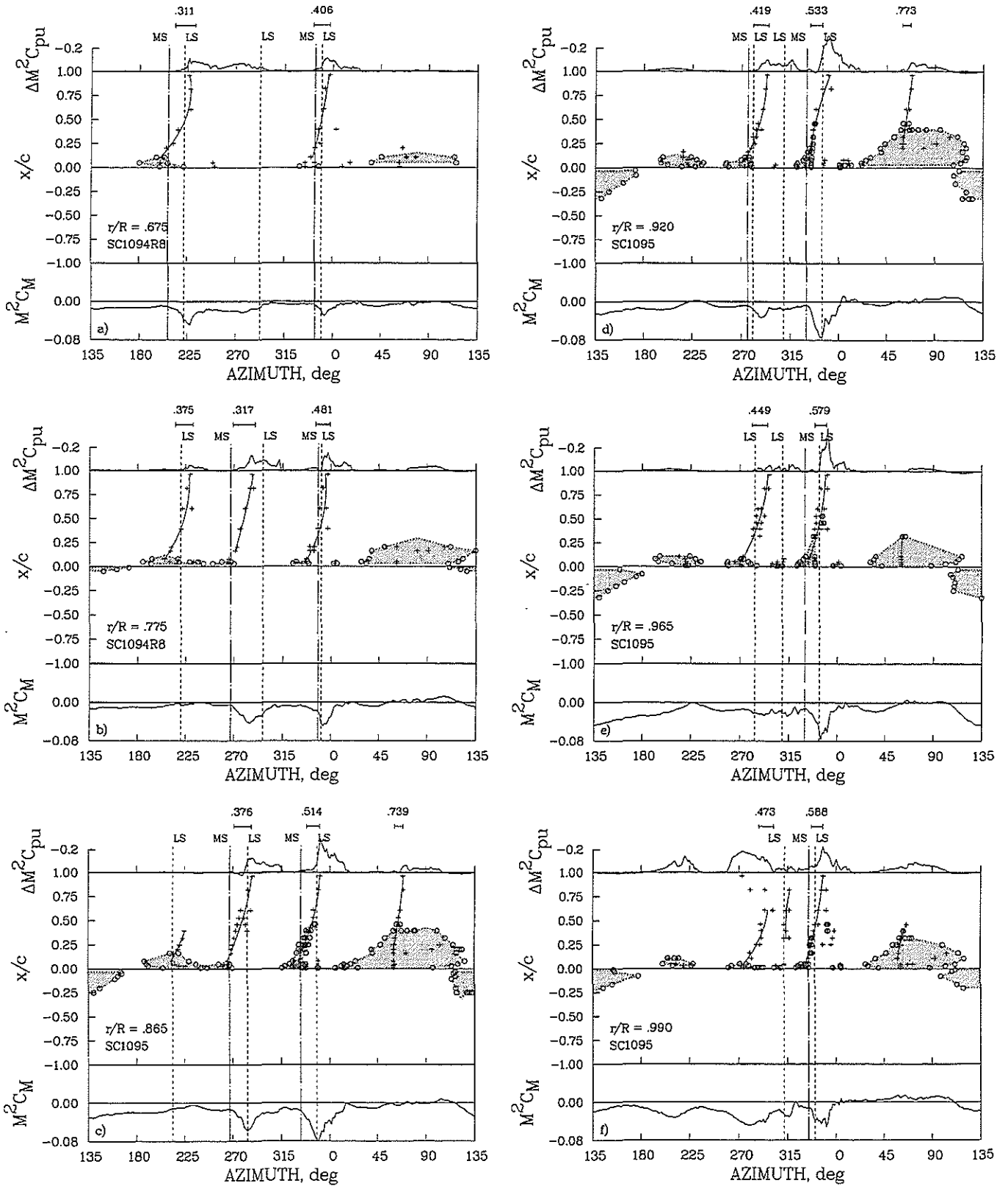


Figure 12. Airfoil map for UTTAS pull-up; Rev 22.

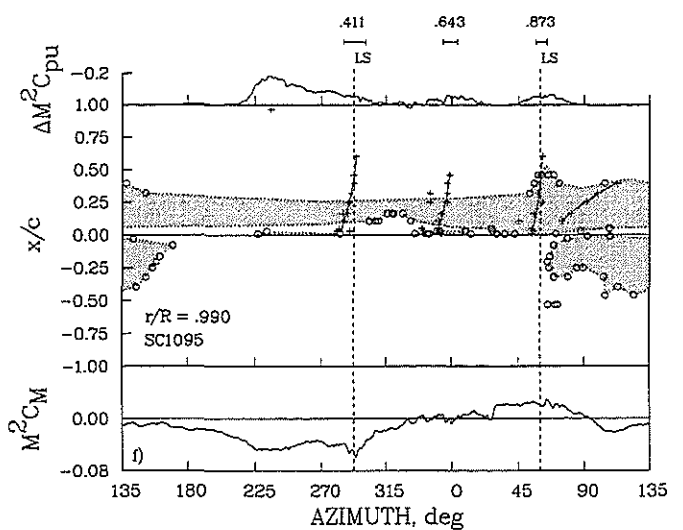
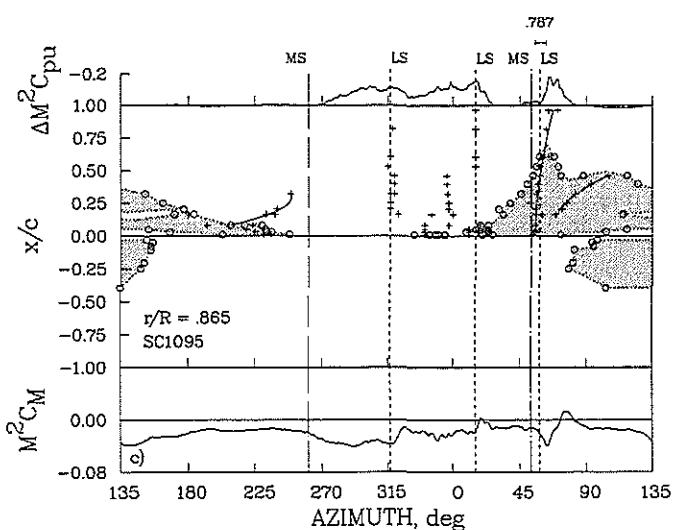
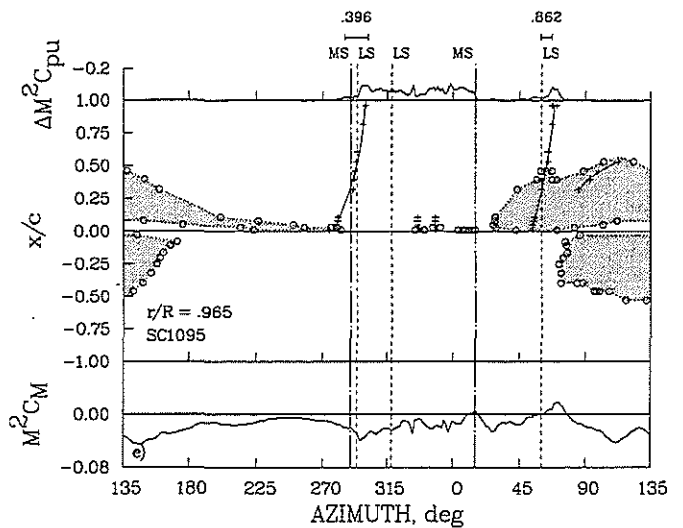
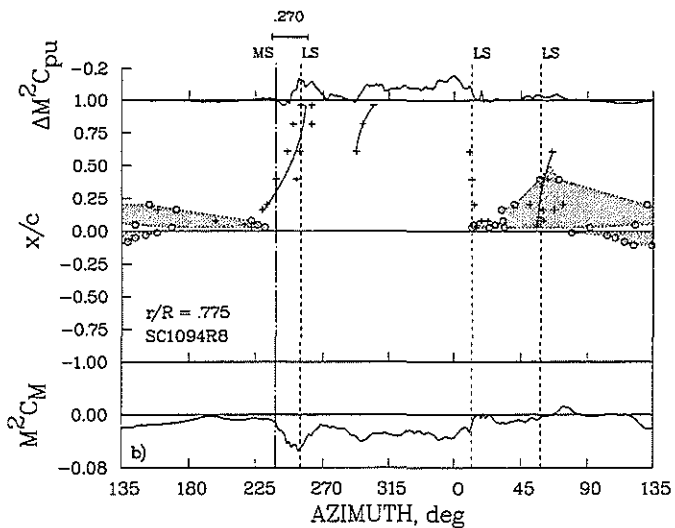
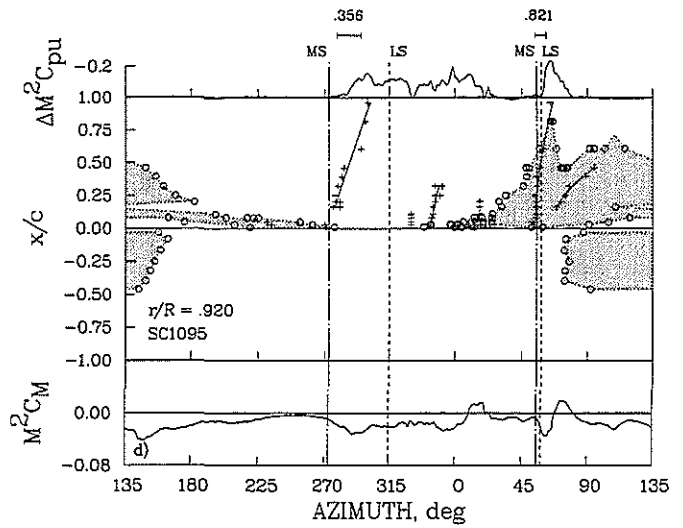
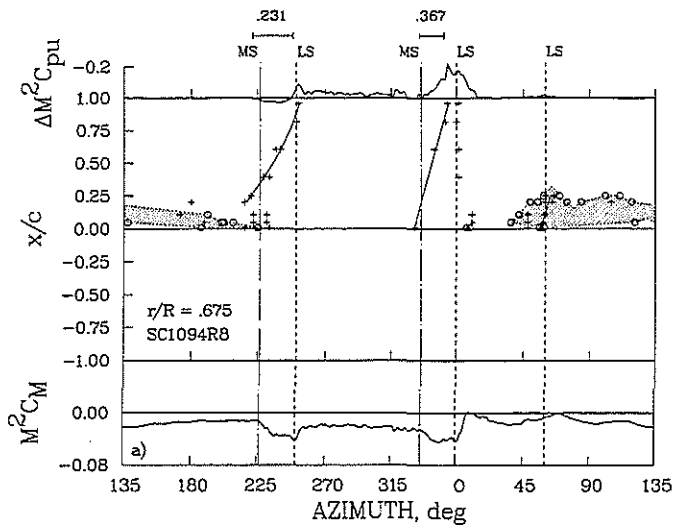


Figure 13. Airfoil map for high-speed, diving turn; Rev 20.

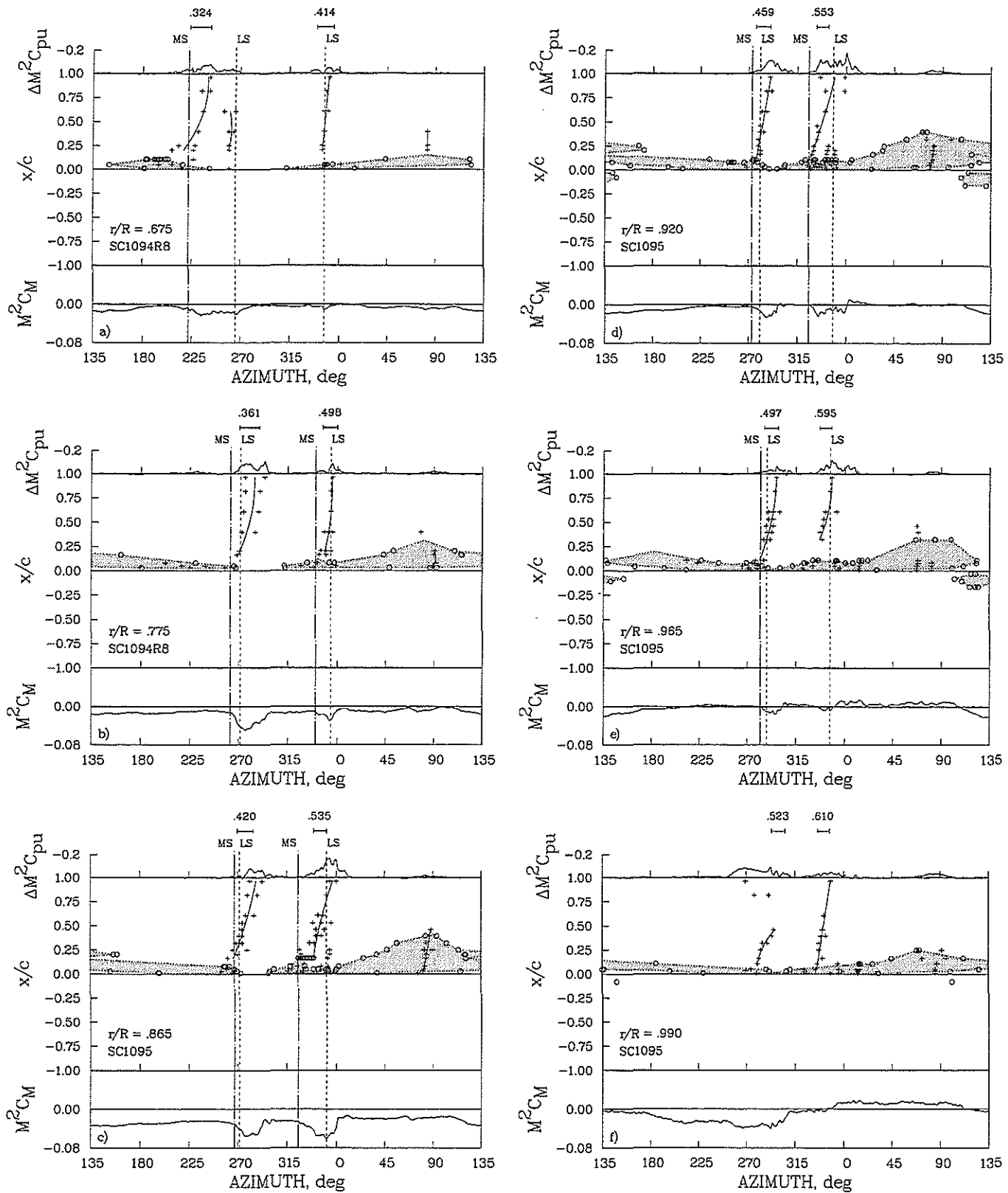


Figure 14. Airfoil map for steady, level flight; Rev 01.

cases examined, the loading at the tip is more strongly affected by separated flow associated with the blade's tip vortex than with the dynamic stall.

### Discussion of Dynamic Stall on the Blade

The detailed investigation of dynamic stall on the blade using the airfoil maps in Figs. 11-14 reemphasizes a number of the conclusions that were obtained from the rotor disk maps. The airfoil maps confirm that dynamic stall on the rotor has many of the same features as seen in 2D wind tunnel tests and this relationship is, perhaps, seen more easily with these maps. The multiple dynamic stall cycles and their repetitive nature is also apparent with the airfoil maps. In addition, the airfoil maps provide more quantitative information about these dynamic stall cycles. The severity of the dynamic stall can be judged from the airfoil maps by the amount of trailing edge separation and the size of the pitching moment and this amplitude information is a valuable adjunct to the rotor disk maps. The airfoil maps also provide new information about the dynamic stall environment, or which, the most interesting perhaps is the range of onset Mach numbers. The Mach number along the blade varies from 0.3 to 0.5 for the first or second stall cycles and although most 2D wind tunnel test data have been obtained at lower Mach numbers, there are a number of experimental studies that cover this range. The onset Mach number for the third dynamic stall cycle, however, exceeds 0.8 in some cases and this is largely outside of the range of 2D wind tunnel test experience. The interaction of the dynamic stall vortex and the supercritical flow in this third cycle is quite complicated and is certainly less easily understood than the characteristics of the earlier cycles at lower Mach numbers.

The formation of the dynamic stall vortex in the first or second stall cycle is often associated with a small area of supercritical flow over the leading edge of the airfoil. The onset Mach numbers for these conditions are well within the range of 2D wind tunnel test experience and it may well be that work in this area will aid in improving models of the dynamic stall process in compressible flows.

The dynamic stall vortex locations defined by the passage of the dynamic stall vortex past the 0.50c position can be mapped onto the rotor plane and these data may more accurately characterize the dynamic stall cycles than the rotor disk maps previously shown. Figure 15 provides a map of these events for all of the cases examined in this paper. The vortex locations are tightly grouped, particularly for the stall vortices at the end of the fourth quadrant (second stall cycle) and on the advancing side of the first quadrant (third stall cycle). At these two latter locations the azimuth of the dynamic stall vortex passage changes only slightly with radial location and little difference is observed for the different cases despite the significant differences in flight condition. The first grouping of dynamic stall vortex azimuths, however, appears to be significantly affected by radial location.

The pattern of the dynamic stall vortex locations indicates that the blade and control system torsional

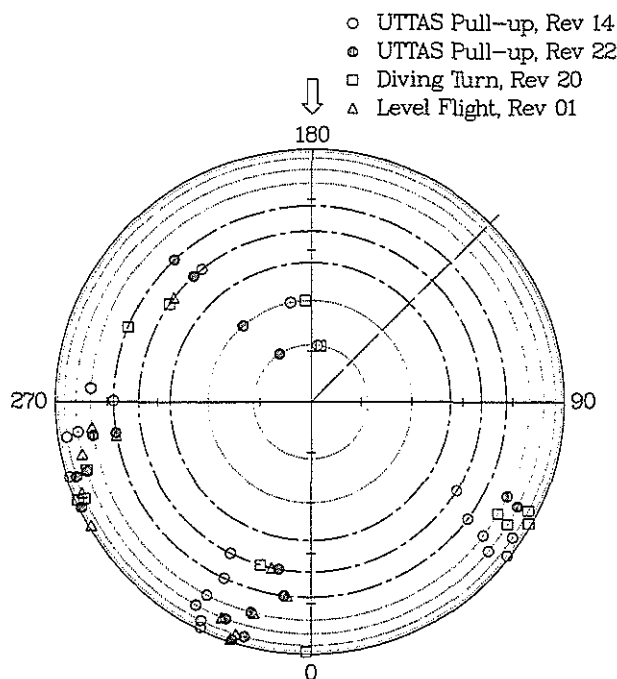


Figure 15. Rotor map of dynamic stall locations for all conditions.

dynamics governs the location of the formation and shedding of the dynamic stall vortices on the rotor through the elastic torsional deformation. This is not altogether surprising. Whether a dynamic stall vortex is actually formed and shed at one of these locations, however, depends upon the inflow distribution and, as has been shown in Figs. 11-14, vortex shedding occurs in some flight conditions but not in others.

### Conclusions

Three flight conditions from the UH-60A Airloads Program have been examined qualitatively to better understand the occurrence of dynamic stall on this rotor. These conditions include a symmetric pull-up maneuver which includes non-zero angular rates and accelerations; a high-speed, diving turn that includes non-zero angular rates, but nominally has zero angular accelerations; and a level flight case where the angular rates and accelerations are zero. Of the three case examined, two represent maneuvers of extraordinary severity for this aircraft and may be considered typical design conditions for this military vehicle. From the examination in this paper the following conclusions are drawn.

1. Dynamic stall, that is, blade stall where a vortex is formed near the leading edge of the airfoil, passes along the upper surface, and then leaves the trailing edge, is clearly seen in all of the flight conditions. The dynamic stall behavior is essentially the same as dynamic stall observed in 2D wind tunnel tests with an abrupt reduction in the

pitching moment as the vortex is formed (moment stall), and a negative peak in the moment as the vortex leaves the trailing edge. The lift is maintained while the vortex passes over the blade, but lift stall occurs as the vortex leaves the airfoil.

2. Multiple dynamic stall cycles are observed on this rotor for most conditions. In many cases three cycles are observed.

3. The dynamic stall vortex appears to be a continuous structure along the length of the blade and in most cases is clearly present at the blade tip. For this aircraft, the initial dynamic stall cycle is observed inboard and moves out to the tip and, in this sense, the dynamic stall vortex inboard has already been shed while it is just being formed outboard. For subsequent stall cycles, however, the formation and shedding of the dynamic stall vortex occurs over the outer blade simultaneously.

4. The location of the dynamic stall vortices occurs in a simple pattern in terms of azimuth and radial station for this rotor and it is apparent that this pattern is controlled by the torsional dynamics of the blade and control system. When dynamic stall occurs it is always observed at these specific locations, but a stall cycle is not always seen for every location for every flight condition.

5. Under the most severe loading conditions the boundary layer may be fully separated over most of the blade for a full quadrant of the rotor. Despite this separation the blade continues to go through repeated dynamic stall cycles.

6. Dynamic stall occurs inboard on the blade over the nose of the aircraft and this is likely caused by an increased angle of attack in this region resulting from flow over the fuselage. Outboard, however, there is no evidence that dynamic stall depends upon aerodynamic interference of the fuselage.

7. Onset Mach numbers range from less than 0.3 inboard on the blade for the first cycle to over 0.8 near the blade tip for the final dynamic stall cycle that occurs in the first quadrant.

8. In the majority of cases the initial formation of the dynamic stall vortex is associated with supercritical flow near the leading edge of the airfoil indicating a close interaction of compressible flow characteristics with the dynamic stall phenomenon.

9. The third dynamic stall cycle that occurs in the first quadrant of the rotor results in the apparent shedding of a dynamic stall vortex at a point where the flow is supercritical over most of the front of the airfoil. It appears that the dynamic stall vortex in this case reduces the surface velocity, but the flow remains supercritical. In this quadrant the dynamic stall event occurs very quickly, perhaps within five or ten deg of azimuth and the exact

details of this high Mach number, high loading condition are not completely clear.

## References

1. McCroskey, W. J., "Some Current Research in Unsteady Fluid Dynamics—The 1976 Freeman Scholar Lecture," *Journal of Fluids Engineering*, Vol. 99, March 1977, pp. 8–38.
2. Ekaterinaris, J. A., Srinivasan, G. R., and McCroskey, W. J., "Present Capabilities of Predicting Two-Dimensional Dynamic Stall," AGARD CP-552, October 1994.
3. Piziali, R., "An Experimental Investigation of 2D and 3D Oscillating Wing Aerodynamics for a Range of Angle of Attack Including Stall," NASA TM-4632, September 1994.
4. Tan, C. M. and Carr, L. W., "The AFDD International Dynamic Stall Workshop on Correlation of Dynamic Stall Models with 3-D Dynamic Stall Data," NASA TM 110375, July 1996.
5. Kufeld, R. M., Balough, D. L., Cross, J. L., Studebaker, K. F., Jennison, C. D., and Bousman, W. G., "Flight Testing the UH-60A Airloads Aircraft," American Helicopter Society 50th Annual Forum Proceedings, May 1994, pp. 557–578.
6. Kufeld, R. M. and Bousman, W. G., "High Load Conditions on a UH-60A In Maneuvering Flight," American Helicopter Society 51st Annual Forum Proceedings, May 1995, pp. 421–433.
7. McCroskey, W. J., McAlister, K. W., Carr, L. W., and Pucci, S. L., "An Experimental Study of Dynamic Stall on Advanced Airfoil Sections; Volume 1. Summary of the Experiment," NASA TM 84245, July 1982.
8. Gangwani, S. T., "Prediction of Dynamic Stall and Unsteady Airloads for Rotor Blades," American Helicopter Society 37th Annual Forum Proceedings, May 1981, pp. 1–17.
9. McCroskey, W. J., McAlister, K. W., Carr, L. W., Pucci, S. L., Lambert, O., and Indergrand, Lt. R. F., "Dynamic Stall on Advanced Airfoil Sections," *Journal of the American Helicopter Society*, Vol. 26, No. 3, July 1981, pp. 40–50.
10. McHugh, F. J., "What Are the Lift and Propulsive Force Limits at High Speed for the Conventional Rotor?," American Helicopter Society 34th Annual Forum, May 1978.

11. Washuta, K. W. and Stocker, B. P., "Air-to-Air Combat Test (AACT II) Maneuvering Flight Loads for UH-60A and AUH-76 Helicopters," USAAVSCOM TR-86-D-1, April 1986.

12. Kufeld, R. M. and Bousman, W. G., "UH-60A Helicopter Rotor Airloads Measured in Flight," Twenty-second European Rotorcraft Forum Proceedings, September 1996, pp. 20.1-20.14.

13. Pearcey, H. H., Wilby, P. G., Riley, M. J., and Brotherhood, P., "The Derivation and Verification of a New Rotor Profile on the Basis of Flow Phenomena; Aerofoil Research and Flight Tests," RAE Technical Memorandum Aero 1440, August 1972.